nature energy

Article

https://doi.org/10.1038/s41560-026-02122-6

Heat-driven elastocaloric cooling with shape memory films

Received: 11 September 2025

Accepted: 20 July 2026

Published online: 28 August 2026

Check for updates

Yi-Ting Hsiau[1], Shuichi Miyazaki[2], Manfred Kohl[1] & Jingyuan Xu[1]

Efficient thermal management is critical for next-generation energy systems. Elastocaloric cooling with shape memory alloy (SMA) films offers rapid heat transfer, high specific cooling capacity and simple solid–solid heat exchange, but current devices rely on bulky, electrically powered actuators that limit scalability and efficiency. Here we demonstrate a thermally powered shape memory actuator that drives elastocaloric cooling in tailored SMA films, establishing a heat-driven cooling system that can use waste heat or solar thermal energy with reduced electricity demand. Our prototype achieves a temperature span of 12.9 K at the refrigerant film level and 4.0 K at the device level under Joule-heated actuation at 86 °C. When driven by an external heat source, the system maintains a device-level temperature span of 2.2 K, confirming the feasibility of heat-driven elastocaloric cooling. These results mark a step towards electricity-minimized elastocaloric cooling technologies that transform heat into useful cooling.

Cooling and heating account for nearly half of global energy demand[1], and the ongoing miniaturization of electronic and photonic devices makes efficient thermal management increasingly critical. Vapour compression cooling dominates the market, but its reliance on high global warming potential refrigerants accounts for more than 40% of global energy-related CO_2 emissions[2] and its bulky components, such as compressors, make it incompatible with miniaturized systems. Thermoelectric devices have been widely deployed to address the demand for miniaturized cooling[3], but their efficiency is only 10–15% of the theoretical reversed Carnot limit, roughly one-quarter that of modern vapour compression systems[4], which greatly constrains their applicability. Elastocaloric cooling, driven by stress-induced martensitic transformations in shape memory alloys (SMAs) or crystallization transitions in polymers[5–8], has emerged as the most promising alternative[9,10], eliminating volatile refrigerants and offering theoretical efficiencies of up to 84% of the Carnot limit[11].

Most recent research on elastocaloric cooling has focused on bulk SMA geometries for macroscale applications, such as SMA tubes, which are coupled with heat-transfer fluids and regenerator designs to achieve high cooling power and a large temperature span[12,13]. Macroscale elastocaloric devices have already demonstrated temperature spans of up to 75 K and 1,284 W cooling power at zero temperature lift[12,14]. By contrast, for miniature-scale cooling, film geometries offer promising prospects: their small mass and large surface-to-volume ratio enhance heat transfer, enabling higher cycling frequencies (for example, 4 Hz) and a high specific cooling power (SCP) of up to 19 W g^{-1} (refs. 15,16). Moreover, film-based elastocaloric devices can avoid the use of heat-transfer fluids by employing solid-to-solid mechanical contact for heat exchange[17,18], minimizing system complexity and allowing operation in confined spaces. To further enhance performance, cascading can increase the temperature span, while parallelization boosts cooling power, together enabling device upscaling for higher overall output[19,20].

Currently, however, elastocaloric cooling prototypes typically rely on electrically powered actuators, making them electricity-dependent systems that continue to incur indirect CO_2 emissions during operation as most electricity is still generated from fossil fuels. In addition, current devices typically use electromechanical motors or hydraulic actuators as drivetrains to generate the large forces required to load superelastic SMA refrigerants[21–25]. However, high-force actuators are commonly designed for long stroke operation, resulting in relatively low force/displacement ratios (defined here as the ratio between maximum output force and stroke length). In contrast, superelastic SMA refrigerants require stresses on the order of several hundred

[1]Institute of Microstructure Technology, Karlsruhe Institute of Technology, Karlsruhe, Germany. [2]Division of Materials Science, University of Tsukuba, Tsukuba, Japan. e-mail: jingyuan.xu@kit.edu

megapascals while undergoing strain of only a few percent, thereby demanding a high force over limited displacement and corresponding to a high force/displacement ratio. This mismatch in actuator–refrigerant mechanical characteristics, together with the substantial mass of conventional drivetrains relative to thin-film refrigerants, leads to inefficient drivetrain utilization and oversized actuation systems[26,27]. A key challenge, therefore, is to develop elastocaloric cooling systems that minimize electricity dependence while employing mechanically well-matched actuators.

In this work, we developed a film-based, heat-driven elastocaloric cooling prototype by integrating thermally powered shape memory actuator films with superelastic SMA refrigerant films, offering the potential to harness low-temperature heat sources, such as waste heat, to deliver electricity-free cooling. The SMA-based thermal actuator provides an improved force/displacement ratio of 14.5 N mm^{-1}, compared with 1.1 N mm^{-1} for the commercial electromechanical actuator used in this study (Supplementary Note 1), as a result of the intrinsic shape recovery behaviour of high-temperature SMAs, which enables high force generation over a limited stroke without bulky transmission systems[26,28–34]. While a regenerative heat-driven elastocaloric concept has been proposed through thermodynamic modelling and numerical simulations at the macroscopic scale[26], in this study, we experimentally realized thermally powered shape memory actuation directly coupled with a thin-film elastocaloric refrigerant architecture at miniature scale. The integrated prototype achieves a temperature span of 12.9 K at the material level and 4.0 K at the device level under Joule-heated thermal actuation at 86 °C. Operation driven by an external heat source was further validated, achieving a device-level temperature span of 2.2 K. This approach addresses the key limitations of electrically driven systems and illustrates the feasibility of using thermal energy as the driving source for thin-film solid-state elastocaloric cooling.

Construction of a heat-driven elastocaloric cooling system

Our prototype integrates two mechanically coupled units: a thermal actuation unit and a cooling unit (Fig. 1a). Thin-film SMAs were chosen for their high surface-to-volume ratio, which promotes rapid heat transfer and enables efficient cycling. The actuation unit employs a 22-µm-thick TiNi SMA film that generates force through the one-way shape memory effect when heated by thermal input. The cooling unit consists of a 26.5-µm-thick TiNiFe superelastic SMA film that functions as the elastocaloric refrigerant. Heat sinks are attached to both units to enable efficient heat rejection, while a polymer coupling element transfers the actuator force directly to the refrigerant film. The two films are mounted in series on low-friction sliders guided on rails, ensuring precise longitudinal motion (Fig. 1b). Further details of device fabrication and construction are provided in the Methods and Supplementary Fig. 1.

The fundamental concept of this work is to combine the shape memory effect and superelasticity of SMAs to realize thermally driven actuation for elastocaloric cooling (Fig. 1c). The red curve illustrates the one-way shape memory effect: when pre-strained in the martensitic state (temperature (T) < martensite finish temperature (M_f)), an SMA can generate an actuation force upon heating above the austenite finish temperature (A_f) as it recovers its pre-set length. The blue curve represents the superelastic characteristic of an SMA with A_f below room temperature. Under external loading, these materials undergo a stress-induced martensitic transformation that releases latent heat, while unloading triggers the reverse transformation that absorbs heat. This reversible process constitutes the elastocaloric effect[35].

The operation cycle of the device consists of four steps (Fig. 1d). The labelled orange and light-blue dashed curves in Fig. 1c correspond to the four operating steps, illustrating the thermomechanical behaviours of the actuator (shape memory effect) and refrigerant (superelastic effect) films. Both films are initially pre-strained to enable actuation by the shape memory effect. In step 1, the thermal input raises the actuator film above its A_f temperature, transforming it from martensite to austenite and generating sufficient force to elongate the refrigerant film. This loading induces a stress-driven martensitic transformation in the refrigerant, accompanied by heat release. In step 2, the heated refrigerant film contacts the heat sink of the cooling unit, where the released heat is rejected. In step 3, the actuator film is cooled to ambient temperature via its heat sink, returning to its martensitic state with reduced force. The refrigerant film then recovers to its original length through superelastic unloading, undergoing the reverse transformation and cooling below ambient temperature. In step 4, the cooled refrigerant film contacts the heat source, absorbs heat from the target region and returns to ambient temperature. Repetition of this four-step cycle transfers heat from the cold side (heat source of the cooling unit) to the hot side (heat sink of the cooling unit), thereby establishing a measurable temperature span across the device.

Material characterization

Two different cold-rolled SMA films are used in the prototype: a one-way shape memory $Ti_{50.18}Ni_{49.82}$ film for thermal actuation and a superelastic $Ti_{49.1}Ni_{50.5}Fe_{0.4}$ film for elastocaloric cooling. Fabrication details are provided in the Methods.

The TiNiFe film was characterized under uniaxial tension by infrared (IR) thermography (Fig. 2a). The engineering stress–strain curve (Fig. 2d) shows transformation onset at ~400 MPa and full martensitic transformation at ~470 MPa at 5.2% strain. The corresponding adiabatic temperature change is 19.4 K, measured over the central area of the film to minimize edge effects (Supplementary Fig. 2). The TiNi film was evaluated in a temperature-controlled chamber with integrated Joule heating (Fig. 2b). The stress–strain response (Fig. 2e) demonstrates its strong temperature dependence: at 2% strain, the stress is 150 MPa in the martensitic state (23 °C) and increases to 440 MPa in the austenitic state (83 °C). The orange curve (Fig. 2e) illustrates loading in martensite, followed by Joule heating above the A_f temperature and unloading in austenite, confirming that the large actuation stress is accessible through the shape memory effect.

Differential scanning calorimetry (DSC; Fig. 2f) showed that the TiNiFe film has an A_f temperature of 18.5 °C, ensuring superelasticity at room temperature. The TiNi film exhibits an austenite start temperature (A_s) and A_f of 47.1 and 60.8 °C, respectively, indicating that heating above A_f is necessary to generate sufficient actuation stress, while cooling below A_s is required to fully recover the initial pre-strain. The characterization protocols are described in the Methods.

Based on these measured properties, the coupled force–displacement relationships of the two films were estimated (Fig. 2c). Four characteristic states were identified ((i)–(iv); also see Fig. 2d): (i) the initial pre-strain, (ii) the onset of stress-induced martensitic transformation in the refrigerant film, (iii) the fully transformed state and (iv) the reverse transformation upon unloading. These material-level results provide essential guidance for force–displacement coupling design in the heat-driven elastocaloric cooling device: the diagram shows that with a pre-strain of ~0.5% (corresponding to a displacement of tens of micrometres) on the refrigerant and an actuator stroke on the order of several hundred micrometres delivering a force of a few newtons, the actuator can fully drive the refrigerant film through its transformation plateau.

Subsystem characterization

The thermal actuation and elastocaloric cooling units were investigated separately to evaluate their stand-alone performance.

Thermal actuation unit

The core element of the thermal actuation unit is a one-way shape memory TiNi film actuator (pre-set length 19 mm) pre-strained by 2.7% (Fig. 3a). One end of the film is fixed while the other is coupled to a TiNiFe

https://doi.org/10.1038/s41560-026-02122-6

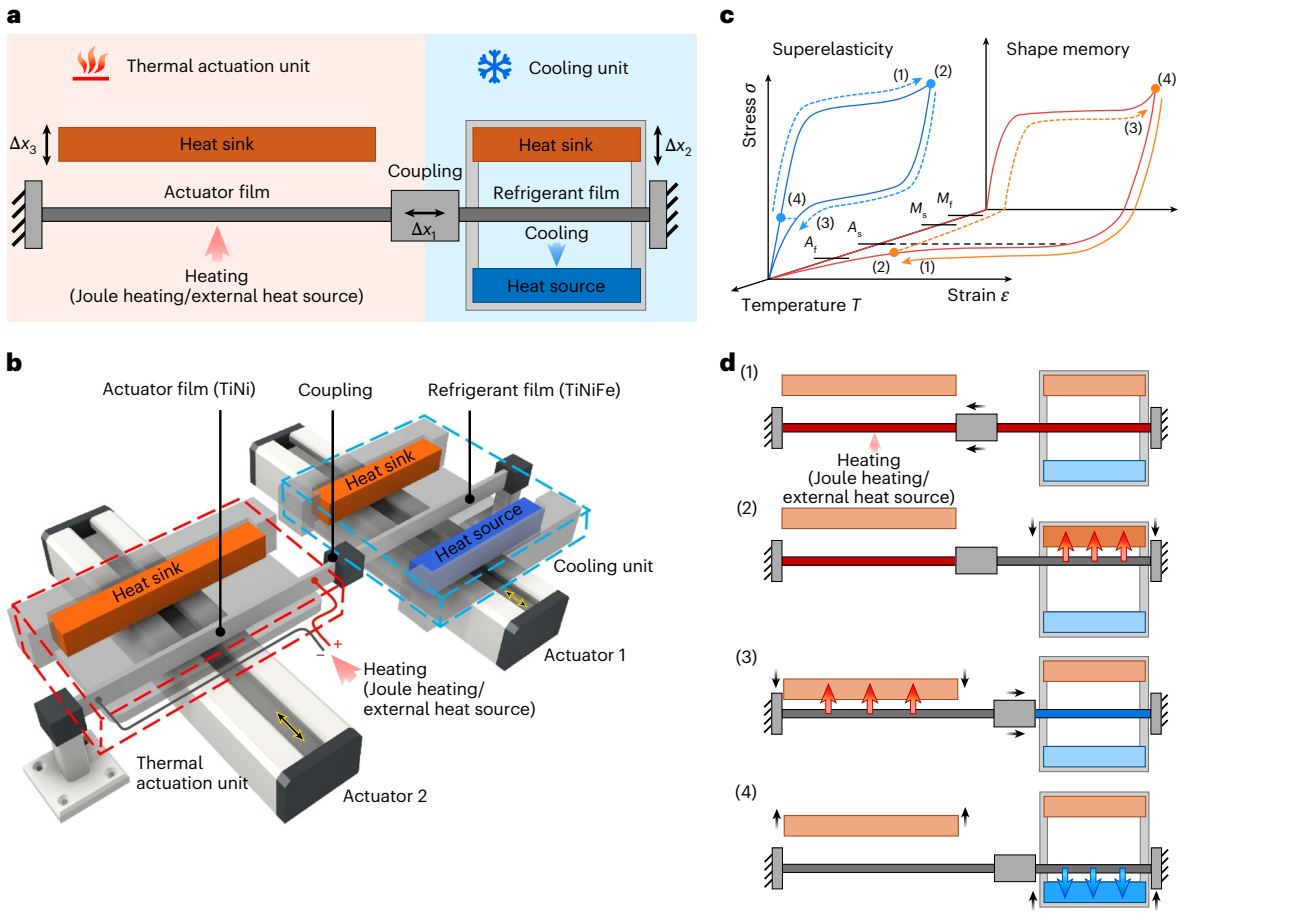

Fig. 1 | Concept and working principle of the heat-driven elastocaloric cooler using SMA films. a, Schematic of the device, comprising a thermal actuation unit (left) and a cooling unit (right), coupled mechanically but thermally isolated. The actuator film (TiNi) is heated to cyclically load and unload the refrigerant film (TiNiFe). Movements Δx_{1-3} indicate the motions of individual components: Δx_1 represents the coupled stroke between the two units, Δx_2 is the motion of the heat sink/source of the cooling unit and Δx_3 is the motion of the heat sink of the actuation unit. **b**, Three-dimensional rendering of the prototype, showing the actuator film, refrigerant film and heat exchangers. The actuator converts absorbed thermal energy into mechanical work that drives the cooling cycle. **c**, Thermomechanical behaviour of SMAs. The actuator operates via the shape memory effect (red), while the refrigerant exploits stress-induced superelasticity (blue). The dashed curves and labelled points correspond to the operation steps in **d**. A_s, austenite start temperature; A_f, austenite finish temperature; M_s, martensite start temperature; M_f, martensite finish temperature. **d**, Schematic showing the four steps of the heat-driven elastocaloric cooling cycle. (1) Thermal input raises the actuator film temperature above A_f (orange curve 1 in **c**), causing contraction and loading the refrigerant film, which undergoes stress-induced austenite–martensite transformation with associated heating (light blue curve 1 in **c**). (2) The refrigerant film contacts the heat sink of the cooling unit, releasing heat until returning to ambient temperature (both points 2 in **c**). (3) The actuator film cools to ambient temperature via its heat sink (orange curve 3 in **c**), unloading the refrigerant film, which undergoes the reverse transformation accompanied by cooling (light blue curve 3 in **c**). (4) The refrigerant film contacts the heat source, absorbing heat and returning to ambient temperature (both points 4 in **c**). The external heat-source-driven configuration is illustrated in Supplementary Fig. 15.

superelastic film serving as a bias spring. During operation, a copper heat sink mounted on an electromechanical actuator periodically contacts the TiNi film to enable controlled cooling. Joule heating above A_f produces strokes of 368–415 µm as pulse time increases (Fig. 3b). The corresponding actuation forces remain above 5.5 N across all conditions, sufficient to fully drive the phase transformation of the TiNiFe refrigerant film, as corroborated by its stress–strain behaviour (Fig. 2d). Loading times remain above 500 ms and show no clear dependence on pulse duration at a Joule heating current of 1.0 A (Supplementary Fig. 3a). In contrast, passive cooling via the heat sink greatly reduces unloading times from >3 s to <1 s (Supplementary Fig. 3b). These results confirm that the thermal actuator delivers both the displacement and force necessary for device operation.

Elastocaloric cooling unit

To assess the stand-alone performance of the cooling unit, the thermal actuator was replaced with an electromechanical actuator to precisely control displacement (Fig. 3c). In this configuration, the heat sink and heat source elements are moved independently to separate thermal flows. Tests were conducted at strains of 4% and 4.5% across frequencies of 1, 1.33 and 2 Hz, with loading/unloading and holding times varied between 125 and 250 ms. Figure 3d shows that larger strain amplitudes yield larger temperature spans, while higher operating frequencies suppress parasitic heat loss and improve cooling performance. Shorter loading/unloading times have a greater impact than shorter holding times, as the higher strain rate in the refrigerant material enhances the adiabatic response. The maximum temperature span achieved is 8.2 K (mean value of three independent measurements) under zero cooling power conditions at 2 Hz and 4.5% strain. By maintaining the heat sink temperature within 1.0 K above ambient, representing a more application-relevant boundary condition, the cold-side temperature drop ($\Delta T_c = T_c - T_0$, where T_c is the cooling temperature in the cooling unit and T_0 is the ambient temperature) increases by an average of 0.8 K compared with the insulated configuration (Supplementary Fig. 4).

https://doi.org/10.1038/s41560-026-02122-6

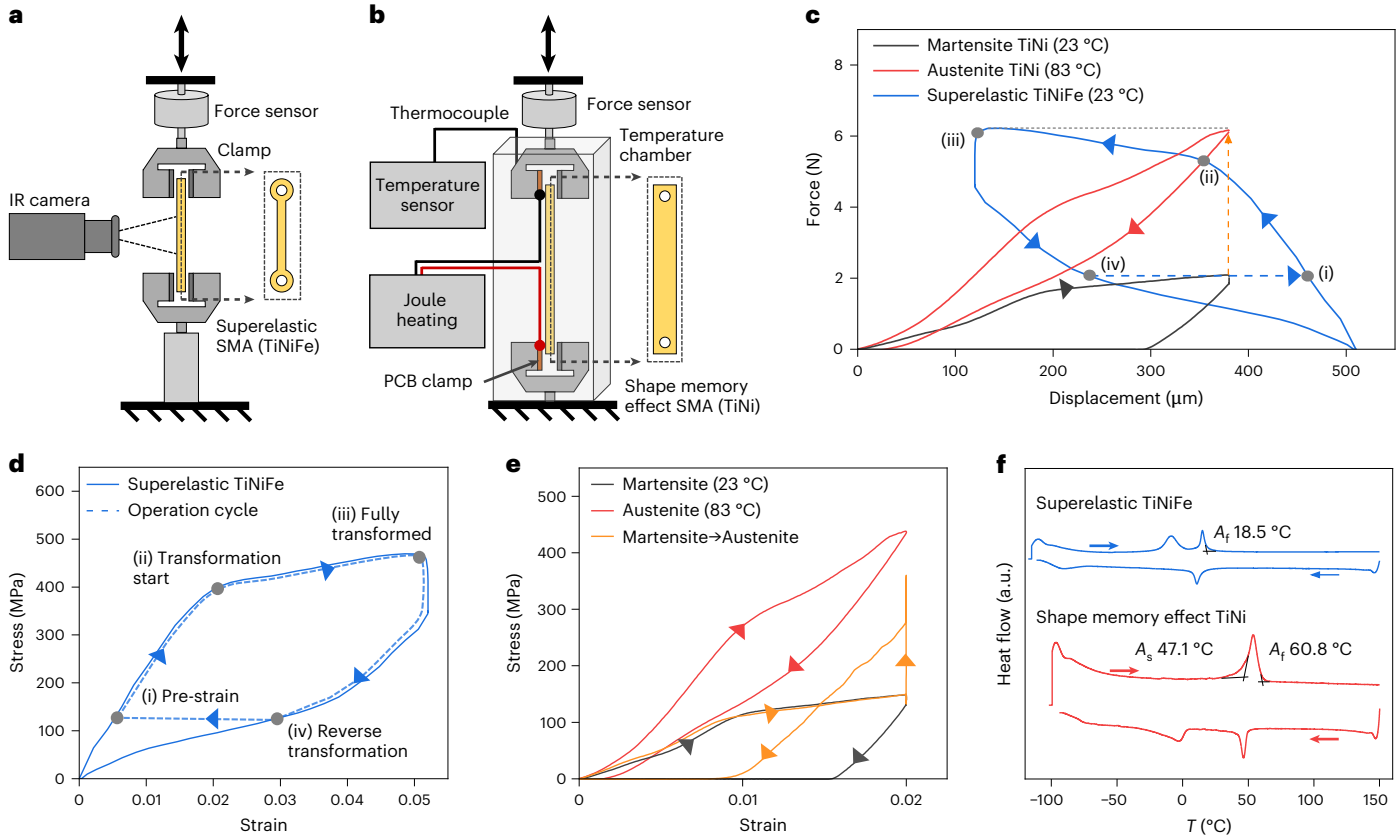

Fig. 2 | Material characterization of the $Ti_{50.18}Ni_{49.82}$ (one-way shape memory) and $Ti_{49.1}Ni_{50.5}Fe_{0.4}$ (superelastic) films. a, Schematic of the tensile test set-up for the superelastic TiNiFe film. **b**, Schematic of the tensile test set-up for the shape memory effect TiNi film. Printed circuit boards (PCBs) are used at the clamps for Joule-heating electrical connections. **c**, Force–displacement curves for the TiNiFe and TiNi films, derived from tensile tests. The grey circles (i)–(iv) indicate the estimated coupling points of the superelastic TiNiFe film expected in the coupled heat-driven system, corresponding to the transformation states shown in **d**. Horizontal dotted and dashed lines indicate the force matching between TiNi and TiNiFe films. **d**, Engineering stress–strain response of the superelastic TiNiFe film at room temperature. Points (i)–(iv) correspond to the coupling points marked in **c**: (i) pre-strain, (ii) transformation start, (iii) fully transformed state and (iv) reverse transformation. The dashed curve enclosed by points (i)–(iv) highlights the operation cycle expected in the coupled heat-driven device. The tested TiNiFe film had a cross-sectional area of 0.5 × 0.026 mm^2. **e**, Engineering stress–strain characteristics of the one-way shape memory effect TiNi film. For the martensite–austenite transformation, loading occurs in the martensitic state, followed by Joule heating above A_f and unloading in the austenitic state, demonstrating the one-way shape memory effect. The tested TiNi film had a cross-sectional area of 3.0 × 0.020 mm^2. **f**, DSC curves of the TiNiFe and TiNi films. TiNiFe shows an A_f of 18.5 °C, while TiNi exhibits an A_s of 47.1 °C and A_f of 60.8 °C. Downward direction indicates exothermic processes.

Although constraining the hot-side temperature rise reduces the overall temperature span ($\Delta T_{total} = T_h - T_c$, where T_h is the heating temperature in the cooling unit), maintaining the heat sink near ambient prevents an upward shift of the system reference temperature and results in a larger measurable temperature drop relative to ambient conditions. Temperature span values under both insulated and ambient-controlled conditions are summarized in Supplementary Table 1.

Coupled heat-driven system using Joule heating

The actuator and refrigerant films are integrated in-plane using a polymer connector, ensuring thermal isolation while enabling direct transfer of displacement and force (Supplementary Fig. 1). In this configuration, the actuation stroke of the TiNi shape memory actuator uniaxially loads and unloads the TiNiFe refrigerant film. The heat sinks and heat source are cyclically moved into contact with both films, with holding times of 0.5 s to ensure efficient thermal exchange.

The integrated heat-driven system under Joule-heated actuation can continuously operate with actuation stroke lengths exceeding 300 μm (Fig. 4a). A sharp initial drop is followed by much slower degradation, attributed to the high operating frequency that hinders full recovery of the martensite state of the actuator during cooling. The force plateaus confirm the occurrence of stress-induced martensitic transformation in the refrigerant film. The force–displacement ratio of the thermal actuation unit was calculated to be 14.5 N mm^{-1}, which is comparable to the target range (16.0–16.7 N mm^{-1}) and substantially higher than that of a commercially available electromechanical actuator (1.1 N mm^{-1}).

IR thermography verified the elastocaloric effect under Joule-heated actuation. At the material level, without heat exchangers in the cooling unit, the refrigerant film exhibits a temperature span of 12.9 K at strain rates of 0.09 s^{-1} (loading) and 0.03 s^{-1} (unloading; Supplementary Fig. 5). With an integrated heat sink and source, the device achieves a temperature span of 4.0 K (Fig. 4b). The temperature drop ($T_c - T_0$) remains at −1.8 K when switching from an insulated heat sink to a heat sink maintained near ambient temperature (Supplementary Fig. 6a), indicating that under the current operating frequency, additional enhancement of the cold-side temperature drop is not observed. This differs from the cooling-only configuration (Supplementary Fig. 4), where a higher electromechanical actuation frequency makes the heat sink condition a dominant factor. In contrast, in the Joule-heated coupled system, the lower operating frequency and strain rate limit the cooling capacity, reducing the influence of the heat sink condition. The cooling power (CP) at zero temperature lift, determined using the counter-heating method, is 2.79 mW, corresponding to an SCP of 4.43 W g^{-1} (Supplementary Fig. 7a and Supplementary Table 3).

https://doi.org/10.1038/s41560-026-02122-6

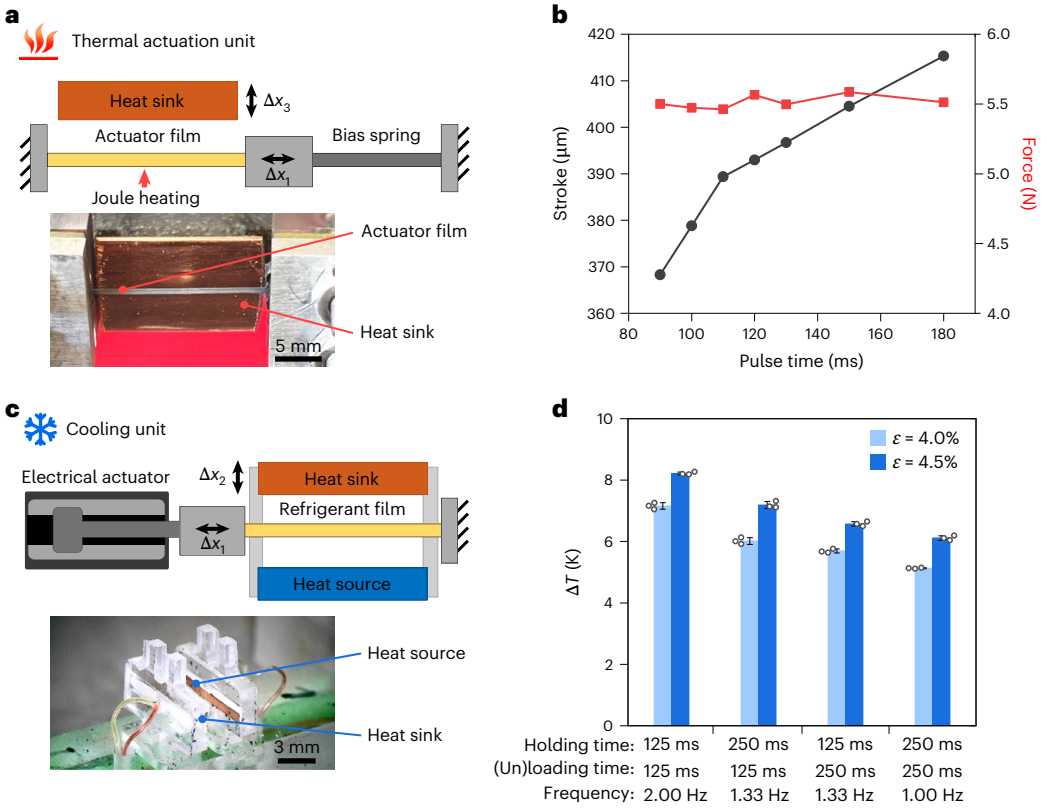

Fig. 3 | Illustration and performance of the thermal actuation and elastocaloric cooling units. a, Schematic and optical image of the thermal actuation unit. The TiNi actuator film is Joule-heated to contract against a bias spring made of a superelastic TiNiFe film. Arrow Δx_1 denotes the stroke of the actuator film and arrow Δx_3 denotes the vertical motion of the heat sink of the actuation unit. **b**, Stroke and output force of the thermal actuation unit operated at 1.0 A heating current for different heating pulse duration (corresponding heating power: 1.32 W). Both actuator film and bias spring were pre-strained with a force of 1.5 N. The symbols represent experimental data; the lines are guides to the eye. **c**, Schematic and optical image of the stand-alone elastocaloric cooling unit driven by a commercial electrical actuator. The TiNiFe refrigerant film is cyclically loaded and unloaded between a heat sink and heat source. Arrow Δx_1 denotes the stroke of the refrigerant film and arrow Δx_2 denotes the vertical motion of the heat sink and heat source of the cooling unit. **d**, Device-level temperature span (ΔT) of the stand-alone cooling unit under imposed strains (ε) of 4% and 4.5%, tested at different (un)loading times (125 or 250 ms) and holding times (125 or 250 ms), corresponding to frequencies of 1, 1.33 and 2 Hz. The maximum ΔT is 8.2 K at 4.5% strain with 125 ms (un)loading and 125 ms holding times. Values under different conditions are given in Supplementary Table 1. The data are shown as mean ± standard deviation (n = 3 independent experiments, shown as white circles).

The actuator film reaches an average peak temperature of 86 °C during cycling (Supplementary Fig. 8), confirming the viability of low-grade heat (<100 °C) as the actuation source. The operations of the cooling and actuation units are shown in Supplementary Videos 1 and 2, while IR thermography footage of the refrigerant film under cyclic operation is provided in Supplementary Video 3.

The motion sequence of the coupled system under Joule-heated actuation is illustrated in Fig. 4c. The longitudinal displacement Δx_1 denotes the coupled stroke transmitted between the actuator and refrigerant films. Point B (~380 μm) marks the full transformation of the refrigerant film, where stress-induced martensite dominates and its temperature rises. Point A (~50 μm) corresponds to the fully unloaded state, where the refrigerant returns to austenite, absorbing heat from the heat source. This recovery allows the superelastic refrigerant to retain its pre-strained length (~50 μm). The lateral motions Δx_2 and Δx_3 represent the displacements of the heat exchangers in the cooling and actuation units, respectively. Both displacements are set slightly larger than the exchanger separations to ensure reliable solid–solid contact, with holding times of 0.5 s applied to enable sufficient heat transfer.

The thermodynamic performance of the coupled system is summarized in Fig. 4d. Based on the CP determined using the counter-heating method, the coefficient of performance (COP) of the cooling unit is 2.61 without work recovery. The temperature-slope method yields a slightly higher COP of 2.88. The COP of the thermal actuator is 3.27×10^{-2}, based on the Joule-heating thermal input. For the Joule-heated coupled system, the system-level COP is 8.53×10^{-2} (counter-heating method) without work recovery. Definitions of COP and the corresponding exergetic efficiencies are provided in Supplementary Note 2 and Supplementary Table 4. Further efficiency gains could be achieved by (1) reducing parasitic thermal losses through improved insulation[36], (2) optimizing heat-transfer interfaces via high-conductivity interlayers and surface finish adjustment to lower contact resistance[37], and (3) tailoring the actuator–refrigerant coupling by employing compliant polymer or metallic linkages to achieve uniform load distribution and minimize frictional and hysteretic losses in the connector[38,39].

Coupled heat-driven system using an external heat source

To verify true heat-driven operation, Joule heating was replaced with an external solid heat source in the actuation unit, enabling direct conductive heating of the actuator film (Fig. 5a,b). The verification prototype was operated using the same film dimensions and cycling frequency as the Joule-heated configuration to allow direct comparison. The external heat source was maintained at 130 °C (T_s) to provide sufficient thermal input for uniaxial loading of ~300 μm of the refrigerant film within a 0.25 s heating interval (Supplementary Fig. 9a). Active motion control of the heat source and heat sink in the actuation unit constrained the loading and unloading durations to ~0.6 s

https://doi.org/10.1038/s41560-026-02122-6

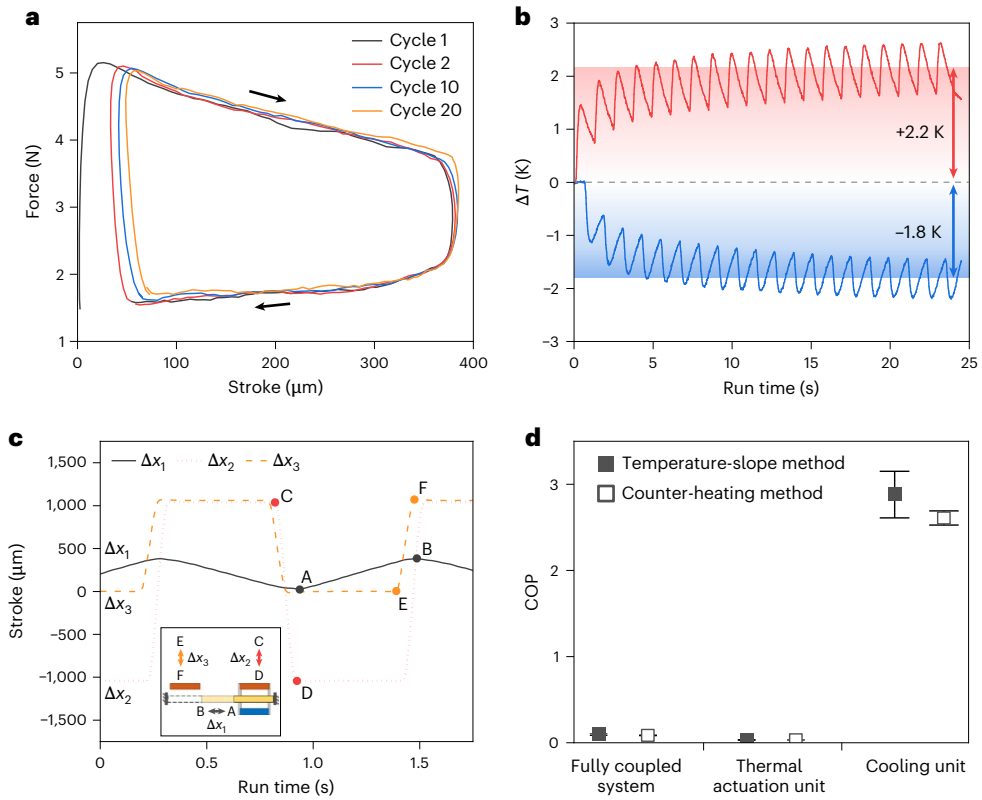

Fig. 4 | Performance of the coupled heat-driven elastocaloric system under Joule-heated actuation. a, Force–stroke loops of the coupled system for cycles 1, 2, 10 and 20. The actuator film undergoes phase transformation driven by Joule heating, and its actuation stroke loads/unloads the refrigerant film, driving the elastocaloric cooling device. A 6-point moving average was applied for readability. **b**, Device-level temperature span (ΔT) over a run time of 24 s. After 20 cycles, a steady-state temperature span of 4.0 K is reached, comprising an average temperature rise of +2.2 K and drop of −1.8 K. **c**, Coordinated motions of the integrated device. Δx_1 corresponds to the coupled axial stroke between the actuation and cooling unit (between points A and B). Δx_2 corresponds to the movement of the heat sink/source in the cooling unit (between points C and D), switching the thermal contact with the refrigerant film. Δx_3 corresponds to the movement of the heat sink in the actuation unit (between points E and F), regulating the actuator film temperature. The total cycle time is 1.2 s, with a holding time of 0.5 s during thermal contact of the film. Inset: schematic of the coupled motions. **d**, COP at zero temperature lift ($\Delta T = 0$ K) under different evaluation criteria. The full-system COP was evaluated on a thermal input basis, where thermal energy absorbed by the actuator film is taken as the input power. Thermal actuator efficiency is defined as the ratio of mechanical work output to thermal input. All COP values were calculated without work recovery. All COP values are provided in Supplementary Table 4. Exergetic efficiencies and full efficiency definitions are provided in Supplementary Note 2 and Supplementary Table 4. The data are shown as mean ± standard deviation ($n = 3$ independent experiments).

(Supplementary Fig. 9b,c), corresponding to strain rates of between 0.053 and 0.066 s^{-1} (Supplementary Fig. 9d).

The cooling performance was evaluated under these conditions, with the heating time increased to 0.35 s to ensure sufficient thermal input into the coupled heat-driven system using an external heat source. With a slightly reduced stroke (strain ≈ 4.1%), the external-heat-source-driven device achieves a steady-state temperature span of 2.2 K at the same operating frequency as the Joule-heated coupled system (Fig. 5c,d). The CP at zero temperature lift, determined using the counter-heating method, is 2.09 mW, corresponding to an SCP of 3.32 W g^{-1} (Supplementary Fig. 7a and Supplementary Table 3). When the heat sink in the cooling unit is maintained near ambient temperature, the cold-side temperature drop ($T_c - T_0$) increases from −1.0 to −1.4 K (Supplementary Fig. 6b). The operations of the external-heat-source-driven actuation unit and the cooling unit in such a configuration are shown in Supplementary Videos 4 and 5.

Compared with the Joule-heated configuration, the external-heat-source-driven system exhibits reductions of 1.8 K in the temperature span and 1.11 W g^{-1} in the SCP (Fig. 5d), primarily due to the lower achievable stroke under the actuator geometry. The higher required heating temperature of 130 °C, compared with 86 °C in the Joule-heated case, reflects the different heat-transfer mechanisms involved. Joule heating generates volumetric internal heat, whereas the external heat source relies on boundary-driven conduction. Optimization of the actuator geometry and transformation temperature A_f, together with improved heat-transfer design, may reduce the required heat-source temperature and enhance actuation efficiency in future implementations.

The future potential of the film-based, heat-driven elastocaloric cooler extends to a broad range of applications where compact, solid-state and electricity-minimized cooling is essential. For instance, in household electronics, the cooler can be integrated to dissipate heat from central processing units in computers, where the thermal actuator can harvest waste heat from voltage regulator modules to drive refrigerant films for localized cooling (Supplementary Fig. 10a). Similarly, in automotive systems, the device can be configured to manage thermal loads in on-board electronics, with the actuator films potentially powered by waste heat sources such as exhaust or drivetrain heat, to deliver targeted cooling of sensitive components (Supplementary Fig. 10b). The present prototype serves as a proof-of-concept platform for investigating the scalability of film-based, heat-driven elastocaloric cooling. Although the absolute CP is limited by the small active mass of the thin-film refrigerant, the total cooling capacity can be increased by (1) integrating multiple films in parallel and (2) enlarging the lateral dimensions of each film, as previously demonstrated for film-based

https://doi.org/10.1038/s41560-026-02122-6

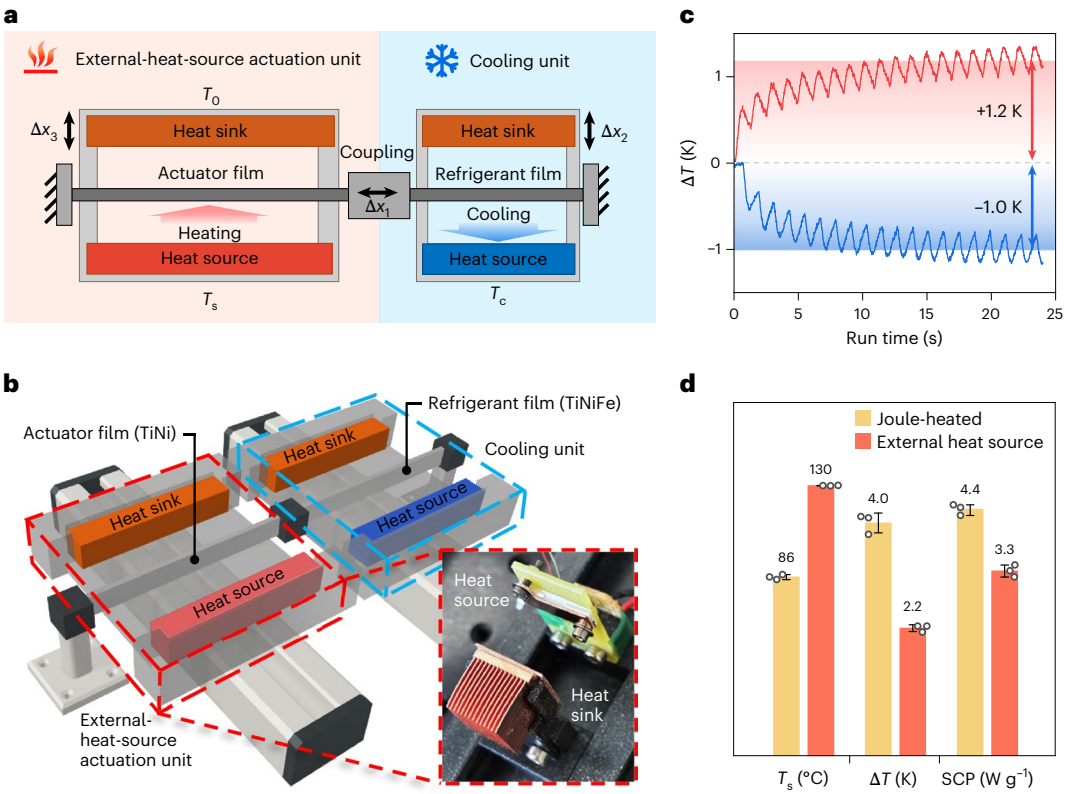

Fig. 5 | System design and performance of the elastocaloric cooling device under external-heat-source actuation. a, Schematic illustration of the device architecture in which Joule heating is replaced by an external solid heat source in the actuation unit, enabling thermal energy input through solid-to-solid contact. **b**, Three-dimensional representation of the prototype, showing the actuator film, refrigerant film, external heat source in the actuation unit and heat exchangers. Inset: close-up view of the fin-structured heat sink and the heat source assembly in the actuation unit. The heat source consists of a platinum microheater bonded to a thin Cu contact plate that interfaces with the actuator film. **c**, Device-level temperature span (ΔT) over an operation period of 24 s. After 20 cycles, a steady-state temperature span of 2.2 K is reached, corresponding to an average temperature rise of +1.2 K on the hot side and an average temperature drop of −1.0 K on the cold side. **d**, Comparison of heating temperature (T_s), temperature span (ΔT) and SCP (counter-heating method) under Joule-heated and external-heat-source actuation. The proof-of-concept external-heat-source configuration exhibits a lower performance, primarily due to the reduced actuation stroke under the current geometric constraints. The data are shown as mean ± standard deviation ($n = 3$ independent experiments, shown as white circles).

elastocaloric systems[19]. As the CP scales approximately with the volume of actively cycled material under comparable stress and strain conditions, increasing the number or area of films can proportionally enhance the total output. In the present architecture, modular integration with shared heat sinks and heat sources may mitigate footprint growth compared with duplicating complete device assemblies. However, scaling to higher cooling capacities requires careful management of heat delivery as larger systems involve increased thermal loads. This necessitates optimized heat-distribution pathways to ensure uniform temperature fields and efficient operation. Potential mitigation strategies include the use of high-conductivity intermediate thermal layers to homogenize temperature distribution, enhanced heat-transfer interfaces to reduce thermal resistance or modular architectures that minimize heat-transport distances by locally coupling heat sources and active elements. In addition, actuator synchronization and uniform stress distribution across multiple films must be addressed. These aspects are not yet implemented in the current prototype and will require further investigation and engineering development in future work.

Conclusions

Here we have presented an integrated film-based, heat-driven elastocaloric cooler that converts thermal energy into mechanical work to drive solid-state refrigerants. By leveraging thin-film SMA architectures for both actuator and refrigerant, the design maximizes the surface-to-volume ratio, enabling rapid heat transfer and a high SCP. Through in-plane coupling of TiNi actuator films with TiNiFe refrigerant films, the Joule-heated configuration achieves continuous cyclic operation with material-level temperature spans of up to 12.9 K and device-level spans of 4.0 K, corresponding to an SCP of 4.4 W g^{-1} at a heating temperature of 86 °C. When driven by an external heat source instead of Joule heating, the system maintains a device-level temperature span of 2.2 K with an SCP of 3.3 W g^{-1} at a heating temperature of 130 °C. These results demonstrate the feasibility of film-based, heat-driven elastocaloric cooling and highlight the potential of thermal energy as a driving source for electricity-minimized thermal management systems.

Methods

Device fabrication

Detailed architecture designs of the prototype are provided in Supplementary Fig. 1. The heat sink in the actuation unit was mechanically cut from a 750-µm-thick Cu plate in a rectangular geometry (18 × 13 mm^2). The surface was manually polished with polishing paper and metal paste to reduce contact resistance. It was attached to a 3D-printed cantilever structure to improve contact with the actuator film. The spring-like compliant cantilever mitigates film–heat exchanger misalignment and preserves stable thermal contact, even under minor buckling of SMA films.

The heat sink and heat source in the cooling unit were fabricated from 100-µm-thick Cu sheets by laser cutting into 7.0 × 0.5 mm^2 strips.

Surfaces were manually polished. A 350-µm-thick aerogel thermal insulation layer (Stanford Advanced Materials) was cut to the same size and adhered to the backside of the Cu heat exchangers. The performance of the insulation layer is shown in Supplementary Fig. 11, confirming its positive effect in maintaining heat exchanger temperature. The heat exchangers were glued to a polymethyl methacrylate (PMMA) support structure. A central hole in the PMMA allowed a miniature type-K thermocouple to be attached to the backside of the Cu sheet with thermally conductive glue. Polydimethylsiloxane (PDMS) square rings were placed around the PMMA support legs before assembly with the top and bottom PMMA plates to provide compliance. This design mitigates the effects of minor buckling in the refrigerant film and ensures stable, repeatable contact with the heat exchangers during operation. The heat sink and source were fixed 2 mm apart and moved together with the plates by an electromechanical linear actuator.

To clamp the refrigerant SMA films, PMMA blocks with a locating pin and hole ensured precise alignment. Two screws secured the films. For the actuator films, the bottom PMMA block was replaced with a PCB board to provide electrical connection for Joule heating. One side of the refrigerant film was clamped and screwed to a linear stage (Norelem; Supplementary Fig. 1, label A) for pre-straining at the beginning of operation.

The two SMA films were mechanically linked by a 3D-printed polymer coupler. The rigid structure ensured that the output force and stroke from the actuator unit were efficiently transferred to the cooling unit. Sliders mounted on the coupler guided motion along the longitudinal axis, reducing parasitic losses and concentrating the applied force. The polymer material and spacing of the coupler further provided effective thermal isolation between the two films.

Material fabrication and characterization

$Ti_{50.18}Ni_{49.82}$ and $Ti_{49.1}Ni_{50.5}Fe_{0.4}$ films were fabricated by cold rolling at the University of Tsukuba, Japan, with 40% reduction to produce ~30-µm-thick films[18,40]. The TiNi films were heat-treated in a vacuum furnace at 450 °C for 30 min to obtain the one-way shape memory effect[41]. Samples were patterned by photolithography and $HF–HNO_3$ wet etching. Actuator films were cut into 19.0 mm (active length) × 0.6 mm strips, followed by $HF–HNO_3$ etching to remove oxides and thinned to 22 µm. The TiNiFe films were laser cut and electropolished (final thickness: 26.5 µm) at ADMEDES. The refrigerant film consisted of a 13.0-mm-long strip with ring-shaped ends, as shown in the inset of Fig. 2a. Each ring had an inner diameter of 1.0 mm and an outer diameter of 2.5 mm, providing precise alignment during clamping. The rectangular gauge section between the two rings was 7.5 mm long and 0.5 mm wide. Scanning electron microscopy images before and after electropolishing are provided in Supplementary Fig. 12, showing substantial surface improvement. A heat treatment at 500 °C for 30 min was required to obtain superelasticity at room temperature[18].

Mechanical properties were measured by means of uniaxial tensile tests on a ZwickRoell Z0.5 testing machine. TiNiFe samples were trained for 20 cycles at a low strain rate (0.001 s^{-1}) until their behaviour was stabilized. The TiNi samples were characterized in the martensite (23 °C) and austenite (83 °C) states in a temperature chamber. Polymer clamp extensions minimized heat loss and an additional thermocouple was attached near the sample to confirm test temperatures.

The fatigue behaviour of the superelastic TiNiFe refrigerant film was evaluated under tensile loading at 5.2% strain and a strain rate of 0.02 s^{-1}. The film sustained more than 2,000 cycles without mechanical failure or observable functional degradation, confirming its mechanical robustness within the operating strain range of the present prototype. However, the primary objective of this work was to establish a proof-of-concept demonstration of heat-driven elastocaloric cooling rather than to optimize long-term cyclic lifetime. Consequently, fatigue-optimized SMA compositions were not specifically implemented in the current device. Notably, ultra-low-fatigue TiNi-based thin films have been reported in the literature. Ti-rich TiNiCu and TiNiCuCo films have demonstrated stable cyclic performance exceeding 10^7 cycles under tensile actuation without functional degradation[42–44]. These alloy systems are fully compatible with thin-film elastocaloric architectures. Combined with an improved mechanical design to minimize stress concentration and thermal accumulation, they provide a clear pathway towards substantially extending operational lifetime in future device generations.

IR thermography was performed with a FLIR A655sc camera at 50 fps (640 × 480 pixels, 17 µm pitch, maximum 200 fps). A black paint spray (emissivity: 0.97) was applied to SMA films before measurement. DSC was performed using a Netzsch Phoenix DSC 204 instrument at a heating rate of 10 °C min^{-1} across temperature ranges of −120 to 150 °C for TiNiFe and −100 to 150 °C for TiNi.

Device characterization

Characterization of subsystems. The prototype was first evaluated at the subsystem level to isolate the performance of the actuation and cooling units.

In the actuation-only unit, TiNi films were Joule-heated under controlled pre-strain to study displacement and force generation. One end of the film was fixed, while the other was coupled to a TiNiFe superelastic film that functioned as a bias spring to enable cyclic operation. At the beginning of testing, both films were pre-strained with a force of 1.5 N, corresponding to a pre-strain length of 520 µm (ε = 2.7%) for the 19-mm-long actuator film. Joule heating pulses of 0.9–1.0 A with durations of between 90 and 180 ms were applied. Higher heating currents and longer pulse durations were not tested to prevent overheating of the actuator film and polymer clamping structures, as well as to avoid excessive heat accumulation that would prolong the subsequent cooling stage. With a pre-strain of 770 µm (ε = 3.2%), the shortest achieved loading and unloading cycle was 500 and 530 ms, respectively, using a 24 mm actuator film under 0.9 A and 90 ms pulses.

In the cooling-only unit, the thermal actuator was replaced with a precision electromechanical actuator to directly control the displacement of the TiNiFe refrigerant film. A second independent electromechanical actuator was used to cyclically move the heat sink and heat source, thereby modulating thermal contact and heat exchange. Strain amplitudes of 4–4.5% were applied at operating frequencies of 1, 1.33 and 2 Hz, with loading/unloading and holding times varied between 125 and 250 ms.

Device-level temperature spans were measured using miniature type-K thermocouples (tip diameter: 360 µm; sensing wire diameter: 80 µm) attached at the centre of the heat sink and heat source (denoted as TC_{mid} in Supplementary Fig. 13a). To verify that TC_{mid} accurately represents the overall heat-source temperature, an additional thermocouple (TC_{side}) was placed near the edge of the heat source. The temperature difference between TC_{mid} and TC_{side} remained below 0.1 K throughout operation (Supplementary Fig. 13b), confirming a spatially homogeneous temperature distribution across the heat source during cycling.

Coupled heat-driven system with Joule-heated actuation. After subsystem evaluation, the actuator and cooling unit were integrated to form a coupled heat-driven system operated using Joule heating. In this configuration, the actuation stroke of the TiNi actuator film directly loaded and unloaded the TiNiFe refrigerant film via a polymer connector, ensuring thermal isolation while enabling efficient force transfer. The heat sink and heat source were cycled laterally into contact with the refrigerant film, while a second heat sink contacted the actuator film to regulate its temperature. A holding time of 0.5 s was applied during each thermal contact to allow sufficient heat exchange.

System control and data acquisition were carried out using a National Instruments cRIO-9067 CompactRIO controller running a custom LabView project. The force of the superelastic refriger

ant film was measured using a U9C 100 N load cell (HBM; label B in Supplementary Fig. 1), and its axial displacement was recorded with a Panasonic HL-G103-S-J laser displacement sensor (label C in Supplementary Fig. 1). IR thermography was used to monitor the film-level temperature response, with carbon spray (emissivity: 0.77) applied to ensure uniform emissivity. Device-level temperature spans were acquired with miniature type-K thermocouples attached to the Cu heat sink and source. The input electrical power for Joule heating of the actuator was supplied by a GW Instek GPP-3060 DC power source, with pulse timing regulated by an external relay module controlled from LabView. Four-wire measurement was used to monitor the supplied electrical power. The electromechanical actuators used for the lateral motion of the heat sink and heat source of the cooling unit and the heat sink of the actuator unit were two servo linear actuators (ESR Pollmeier), operated via the EtherCAT protocol and logged through the CompactRIO system.

The integrated system was operated at a frequency of 0.83 Hz. The initial pre-strain of the actuator film was set to 520 µm ($\varepsilon = 2.7\%$) and the Joule heating pulse was supplied with a current of 1.0 A with a duration time of 100 ms. This corresponded to a pre-strain force of 1.5 N, producing a pre-strain of ~50 µm in the refrigerant film. The pre-strain length was kept moderate as larger pre-strains did not improve cooling performance. It also prevented buckling of both SMA films during push–pull operation.

Under these conditions, a maximum material-level temperature change of 12.9 K and device-level spans of up to 4.0 K were achieved. The average heat-transfer times between the refrigerant film and the heat sink and heat source were approximately 270 and 350 ms, respectively, as determined from the temperature evolution of the heat exchangers. The experimentally derived thermal time constant ($\tau \approx 62$ ms) agrees well with the theoretical estimation (see Supplementary Note 3 for details). A stability test performed under Joule-heated actuation over 80 cycles (96 s) showed no degradation in temperature span or maximum loading force. Although a slight reduction in stroke was observed, the minimum value remained above the designed threshold of 300 µm, resulting in a stable cooling performance (Supplementary Fig. 14).

The material-level temperature change of 12.9 K for the TiNiFe films under Joule-heated thermal actuation is lower than the fully adiabatic value of 19.4 K measured under high-strain-rate tensile testing. This reduction arises from the limited strain rate during device operation. Similarly, the device-level temperature span of 4.0 K in the coupled heat-driven configuration remains below the maximum 8.2 K achieved in the cooling-only unit driven by an electromechanical actuator. In both cases, the limitation originates from thermally constrained actuation dynamics, which restrict both the strain rate and the achievable operating frequency. Fully adiabatic conditions typically require strain rates $\geq 0.1\ s^{-1}$ ((un)loading velocity: ~750 µm s^{-1}), whereas the present actuator provides 0.09 s^{-1} during loading (velocity: ~639 µm s^{-1}) and 0.07 s^{-1} during unloading (velocity: ~526 µm s^{-1}). These sub-adiabatic strain rates allow partial heat exchange during phase transformation. At the device level, the temperature span is further limited by finite heat-transfer rates between the refrigerant film and the heat sink/source, as well as by the thermal mass of the heat exchangers during cyclic operation. In the absence of regenerative or cascaded architecture[15,45], the net temperature lift accumulated per cycle remains lower than the intrinsic material temperature change. Future improvements may focus on increasing strain rates through optimized actuator geometry, enhanced heat transfer or alternative actuation strategies to more fully exploit the intrinsic cooling potential of the refrigerant film. Advanced actuation concepts, including bistable configurations, agonist–antagonist designs or catch-and-release mechanisms[46,47], together with multistage cascading architectures on the cooling side[15,45], may further enhance the effective device-level temperature span.

CP was determined using both the temperature-slope method and direct counter-heating measurement. At zero temperature lift, the CPs obtained from the temperature-slope and counter-heating methods were 3.08 and 2.79 mW, respectively (Supplementary Fig. 7a and Supplementary Table 3). The close agreement between these values supports the reliability of the CP evaluation. The slightly lower value obtained from the counter-heating method is attributed to additional thermal leakage to the surroundings under finite temperature-span conditions during counter-heating operation. The COP values at zero temperature lift and exergetic efficiencies at −1.0 K temperature drop, derived using the CP from both methods under different input-power definitions, are summarized in Supplementary Table 4.

Coupled heat-driven system with external-heat-source actuation. The external heat source was fabricated in-house using a $5 \times 5\ mm^2$ platinum microheater (Innovative Sensor Technology). The microheater was bonded with thermally conductive adhesive to a 0.6-mm-thick Cu plate, which served as the contact interface with the actuator film. A thermocouple was attached to the Cu plate for closed-loop proportional-integral-derivative (PID) temperature control. A fin-structured Cu heat sink was employed to remove heat from the actuator film during the cooling stage.

The heat-source temperature was varied between 70 and 130 °C with a 250 ms contact time to determine the heating temperature (T_s) required to achieve sufficient loading stroke and acceptable loading/unloading times (Supplementary Fig. 9). The device operated in a four-step cycle, as illustrated in Supplementary Fig. 15. The operating frequency was set to 0.83 Hz, identical to that of the Joule-heated configuration, for direct comparison. The loading and unloading velocities were 507 µm s^{-1} (strain rate: 0.07 s^{-1}) and 511 µm s^{-1} (strain rate: 0.07 s^{-1}), respectively.

CP was determined using both the temperature slope and direct counter-heating methods. At zero temperature lift, the CPs obtained from the two methods were 1.36 and 2.09 mW, respectively (Supplementary Fig. 7a and Supplementary Table 3). The small difference between the two methods arises from their distinct evaluation principles. In the counter-heating method, the CP is inferred from the electrical power required to maintain thermal balance. Parasitic heat exchange with the ambient environment contributes to the applied heating power, which can lead to a slight overestimation of the CP[48]. In contrast, the temperature-slope method relies on the initial cooling rate of the heat source, which can be influenced by finite thermal response times associated with contact resistance and the thermal mass of surrounding components, resulting in a slight underestimation of the CP[18]. As a result, the two methods exhibit opposite systematic tendencies, leading to a difference between the evaluated values. The COP values at zero temperature lift and exergetic efficiencies at −0.5 K temperature drop, evaluated under different input-power definitions, are summarized in Supplementary Table 4.

Calculation of figures of merit

System performance was evaluated after 20 operating cycles, when the temperature span profiles reached steady state. The device-level temperature span is defined as the temperature difference between the Cu heat sink and heat source in the cooling unit, measured by type-K thermocouples.

CP and SCP were determined using two independent approaches: the temperature-slope method and direct counter-heating measurement. In the temperature-slope method, CP is obtained from the initial temperature decay rate of the heat source during the first cooling cycle at zero temperature lift[18,49]. In the counter-heating method, a calibrated 0.5 Ω NiCr resistance wire is used to electrically supply heat to the heat source until thermal balance is reached, and the electrical input power required to offset the cooling effect is taken as the CP. To establish controlled thermal loading conditions, the heat source was preheated using the resistance wire for 60 s before actuation. Subsequently, the elastocaloric system was activated to induce cooling, while the

electrical heating was maintained throughout the measurement. The resulting temperature evolution under different thermal loads is shown in Supplementary Fig. 7b. All measurements were conducted during a run time of 24 s to ensure consistency with other tests throughout this work. The remaining temperature change rate at the end of the measurement was negligibly small and the temperature span development reached a steady state within the timeframe.

For the temperature-slope method, CP ($\dot{Q}_c$) is given by:

$$\dot{Q}_c = m_{source} c_{p,source} \dot{T}_{source} \quad (1)$$

where m_{source} is the mass of the Cu heat source, $c_{p,source}$ is the specific heat of Cu and $\dot{T}_{source}$ is the initial cooling rate of the heat source extracted from the first cooling cycle at zero temperature lift.

SCP ($\dot{q}_c$) is defined as:

$$\dot{q}_c = \frac{\dot{Q}_c}{m_{SE}} \quad (2)$$

where m_{SE} is the active mass of the refrigerant film, determined from the clamped gauge length (7.5 mm). The numerical values of all parameters used in these calculations are provided in Supplementary Table 2.

COP was evaluated at zero temperature lift under different input definitions using the CP determined by both the temperature-slope and counter-heating methods. Exergetic efficiency (η_{ex}) was evaluated at 50% of the maximum temperature drop (−1 K for Joule-heated operation and −0.5 K for external-heat-source-driven operation) using the CP obtained from the counter-heating method. Detailed definitions and formulations of COP and η_{ex} under all evaluation criteria are provided in Supplementary Note 2, and a complete summary of efficiency values is presented in Supplementary Table 4.

Data availability

The data supporting the findings of this study are included in the article and the Supplementary Information. Source data are provided with this paper.

References

1. Heat is the greatest challenge in tackling climate change. *World Economic Forum* https://www.weforum.org/stories/2023/03/heat-heres-why-its-the-elephant-in-the-room-for-decarbonization/ (2023).
2. Power to heat and cooling: status. *IRENA* https://www.irena.org/Innovation-landscape-for-smart-electrification/Power-to-heat-and-cooling/Status (2023).
3. DiSalvo, F. J. Thermoelectric cooling and power generation. *Science* **285**, 703–706 (1999).
4. Difference between thermoelectric cooler (TEC) and thermoelectric generator (TEG). *Thermal Book* https://thermalbook.wordpress.com/difference-between-tec-and-teg/ (2015).
5. Moya, X., Kar-Narayan, S. & Mathur, N. D. Caloric materials near ferroic phase transitions. *Nat. Mater.* **13**, 439–450 (2014).
6. Xie, Z., Sebald, G. & Guyomar, D. Temperature dependence of the elastocaloric effect in natural rubber. *Phys. Lett. A* **381**, 2112–2116 (2017).
7. Zhang, S. et al. Shearo-caloric effect enhances elastocaloric responses in polymer composites for solid-state cooling. *Nat. Commun.* **15**, 6567 (2024).
8. Kirsch, S.-M. et al. NiTi-based elastocaloric cooling on the macroscale: from basic concepts to realization. *Energy Technol.* **6**, 1567–1587 (2018).
9. VHK & ARMINES *Preparatory/Review Study on Commission Regulation (EC) No. 643/2009 with Regard to Ecodesign Requirements for Household Refrigeration Appliances and Commission Delegated Regulation (EU) No. 1060/2010 with Regard to Energy Labelling of Household Refrigeration Appliances* (European Commission, 2016).
10. *Top 10 Emerging Technologies of 2024* (World Economic Forum, 2024); https://www.weforum.org/publications/top-10-emerging-technologies-2024/
11. Cui, J. et al. Demonstration of high efficiency elastocaloric cooling with large ΔT using NiTi wires. *Appl. Phys. Lett.* **101**, 073904 (2012).
12. Zhou, G. et al. Achieving kilowatt-scale elastocaloric cooling by a multi-cell architecture. *Nature* **639**, 87–92 (2025).
13. Tušek, J. et al. A regenerative elastocaloric heat pump. *Nat. Energy* **1**, 16134 (2016).
14. Zhou, G. et al. A multi-material cascade elastocaloric cooling device for large temperature lift. *Nat. Energy* **9**, 862–870 (2024).
15. Xu, J. et al. SMA film-based elastocaloric cooling devices. *Shap. Mem. Superelasticity* **10**, 119–133 (2024).
16. Bruederlin, F. et al. Elastocaloric cooling on the miniature scale: a review on materials and device engineering. *Energy Technol.* **6**, 1588–1604 (2018).
17. Ludwig, C., Leutner, J., Prucker, O., Rühe, J. & Kohl, M. Miniature-scale elastocaloric cooling by rubber-based foils. *J. Phys. Energy* **6**, 015009 (2023).
18. Bruederlin, F., Ossmer, H., Wendler, F., Miyazaki, S. & Kohl, M. SMA foil-based elastocaloric cooling: from material behavior to device engineering. *J. Phys. D* **50**, 424003 (2017).
19. Ulpiani, G. et al. Upscaling of SMA film-based elastocaloric cooling. *Appl. Therm. Eng.* **180**, 115867 (2020).
20. Bruederlin, F., Bumke, L., Quandt, E. & Kohl, M. Cascaded SMA-film based elastocaloric cooling. In *2019 20th International Conference on Solid-State Sensors, Actuators and Microsystems and Eurosensors XXXIII (TRANSDUCERS and EUROSENSORS XXXIII)* 1467–1470 (IEEE, 2019).
21. Yao, S. et al. Efficient roller-driven elastocaloric refrigerator. *Nat. Commun.* **15**, 7203 (2024).
22. Li, X., Hua, P. & Sun, Q. Continuous and efficient elastocaloric air cooling by coil-bending. *Nat. Commun.* **14**, 7982 (2023).
23. Zhang, J. et al. Sustainable all-solid elastocaloric cooler enabled by non-reciprocal heat transfer. *Nat. Sustain.* **8**, 651–660 (2025).
24. Ahčin, Ž et al. High-performance cooling and heat pumping based on fatigue-resistant elastocaloric effect in compression. *Joule* **6**, 2338–2357 (2022).
25. Qian, S. et al. High-performance multimode elastocaloric cooling system. *Science* **380**, 722–727 (2023).
26. Qian, S., Wang, Y., Yuan, L. & Yu, J. A heat driven elastocaloric cooling system. *Energy* **182**, 881–899 (2019).
27. Wang, Y. et al. Towards practical elastocaloric cooling. *Commun. Eng.* **2**, 79 (2023).
28. Kim, M.-S. et al. Shape memory alloy (SMA) actuators: the role of material, form, and scaling effects. *Adv. Mater.* **35**, 2208517 (2023).
29. Kohl, M. *Shape Memory Microactuators* (Springer, 2004).
30. Tan, J., Wang, Y., Xu, S., Liu, H. & Qian, S. Thermodynamic cycle analysis of heat driven elastocaloric cooling system. *Energy* **197**, 117261 (2020).
31. Qian, S., Yao, S., Wang, Y., Yuan, L. & Yu, J. Harvesting low-grade heat by coupling regenerative shape-memory actuator and piezoelectric generator. *Appl. Energy* **322**, 119462 (2022).
32. Yuan, L. et al. Numerical study of a double-effect elastocaloric cooling system powered by low-grade heat. *Appl. Therm. Eng.* **218**, 119302 (2023).
33. Qian, S. et al. Cascade utilization of low-grade thermal energy by coupled elastocaloric power and cooling cycle. *Appl. Energy* **298**, 117269 (2021).
34. Dong, X., Jiang, X. & Li, P. An efficient low-grade thermal energy dual-driven elastocaloric cooling system: thermodynamic cycle analysis, economic and sustainability assessment. *Energy Convers. Manage.* **324**, 119310 (2025).

35. Engelbrecht, K. Future prospects for elastocaloric devices. *J. Phys. Energy* **1**, 021001 (2019).
36. Wang, Y. et al. A high-performance solid-state electrocaloric cooling system. *Science* **370**, 129–133 (2020).
37. Ossmer, H., Miyazaki, S. & Kohl, M. Elastocaloric heat pumping using a shape memory alloy foil device. In *2015 Transducers—2015 18th International Conference on Solid-State Sensors, Actuators and Microsystems (TRANSDUCERS)* 726–729 (IEEE, 2015).
38. Li, X. et al. High-frequency bending-actuated elastocaloric cooler with enhanced cooling performance. *Cell Rep. Phys. Sci.* **6**, 102669 (2025).
39. Barforooshi, S. D. et al. Thermographic investigation of elastocaloric behavior in Ni-Ti sheet elements under cyclic bending. *Materials* **18**, 3546 (2025).
40. Miyazaki, S., No, V. H., Kitamura, K., Khantachawana, A. & Hosoda, H. Texture of Ti–Ni rolled thin plates and sputter-deposited thin films. *Int. J. Plast.* **16**, 1135–1154 (2000).
41. Jacob, K., Tan, A. S., Sattel, T. & Kohl, M. Enhancement of shock absorption using hybrid SMA-MRF damper by complementary operation. *Actuators* **11**, 280 (2022).
42. Chluba, C. et al. Ultralow-fatigue shape memory alloy films. *Science* **348**, 1004–1007 (2015).
43. Chluba, C., Ossmer, H., Zamponi, C., Kohl, M. & Quandt, E. Ultra-low fatigue quaternary TiNi-based films for elastocaloric cooling. *Shap. Mem. Superelasticity* **2**, 95–103 (2016).
44. Ossmer, H., Chluba, C., Kauffmann-Weiss, S., Quandt, E. & Kohl, M. TiNi-based films for elastocaloric microcooling—fatigue life and device performance. *APL Mater.* **4**, 064102 (2016).
45. Snodgrass, R. & Erickson, D. A multistage elastocaloric refrigerator and heat pump with 28 K temperature span. *Sci. Rep.* **9**, 18532 (2019).
46. Chen, X., Bumke, L., Quandt, E. & Kohl, M. Bistable actuation based on antagonistic buckling SMA beams. *Actuators* **12**, 422 (2023).
47. Bevilacqua, D. et al. Performance analysis of agonist-antagonist SMA micro-wires and resonant compliant joint in bio-inspired bat-like flapping wings. In *Bioinspiration, Biomimetics, and Bioreplication XIV* Vol. 12944, 33–42 (SPIE, 2024).
48. Ziolkowski, P., Blaschkewitz, P. & Müller, E. Heat flow measurement as a key to standardization of thermoelectric generator module metrology: a comparison of reference and absolute techniques. *Measurement* **167**, 108273 (2021).
49. Ludwig, C., Leutner, J., Prucker, O., Ruehe, J. & Kohl, M. Natural rubber foil-based elastocaloric cooling. In *ACTUATOR 2024; International Conference and Exhibition on New Actuator Systems and Applications* 132–135 (VDE, 2024).

Acknowledgements

We thank our collaborators at ADMEDES for support with laser processing and electropolishing of TiNiFe films. We also thank G. Huang for assistance with figure visualization.

Author contributions

Y.-T.H. conceived the idea, built the heat-driven elastocaloric device, performed the experiments and prepared the draft paper. S.M. developed and fabricated the TiNi and TiNiFe films. M.K. contributed to conceptualization, provided resources and revised the paper. J.X. contributed to conceptualization, acquired funding, provided project administration and supervision, and revised the paper. All authors discussed the results and contributed to the final version of the paper.

Funding

J.X. discloses support for the research of this work from the Carl-Zeiss-Stiftung through the CZS Nexus project, the Baden-Württemberg Stiftung through the Elite programme for Postdoctoral Researchers and the Hector Fellow Academy.Open access funding provided by Karlsruher Institut für Technologie (KIT).

Competing interests

The authors declare no competing interests.

Additional information

Supplementary information The online version contains supplementary material available at https://doi.org/10.1038/s41560-026-02122-6.

Correspondence and requests for materials should be addressed to Jingyuan Xu.

Peer review information *Nature Energy* thanks the anonymous reviewer(s) for their contribution to the peer review of this work. Peer reviewer reports are available.